



## Ex situ variable angle spectroscopic ellipsometry studies on chemical vapor deposited boron-doped diamond films: Layered structure and modeling aspects

S. Gupta, A. Dudipala, O. A. Williams, K. Haenen, and E. Bohannon

Citation: *J. Appl. Phys.* **104**, 073514 (2008); doi: 10.1063/1.2990058

View online: <http://dx.doi.org/10.1063/1.2990058>

View Table of Contents: <http://jap.aip.org/resource/1/JAPIAU/v104/i7>

Published by the [American Institute of Physics](#).

---

### Related Articles

Field emission from single-, double-, and multi-walled carbon nanotubes chemically attached to silicon  
*J. Appl. Phys.* **111**, 044326 (2012)

Ceasing of voltage switching amongst graphitic shells in multiwalled carbon nanotubes: A route toward stability  
*Appl. Phys. Lett.* **100**, 043505 (2012)

Directly grown large area single-walled carbon nanotube films with very high sensitivity to normal pressure  
*J. Appl. Phys.* **111**, 023502 (2012)

Magnetoresistance of nanocarbon materials based on carbon nanotubes  
*Low Temp. Phys.* **37**, 819 (2011)

Characterization of the electrical contact between a conductive atomic force microscope cantilever and a carbon nanotube  
*J. Appl. Phys.* **110**, 054305 (2011)

---

### Additional information on *J. Appl. Phys.*

Journal Homepage: <http://jap.aip.org/>

Journal Information: [http://jap.aip.org/about/about\\_the\\_journal](http://jap.aip.org/about/about_the_journal)

Top downloads: [http://jap.aip.org/features/most\\_downloaded](http://jap.aip.org/features/most_downloaded)

Information for Authors: <http://jap.aip.org/authors>

## ADVERTISEMENT



**FIND THE NEEDLE IN THE  
HIRING HAYSTACK**

Post jobs and reach  
thousands of hard-to-find  
scientists with specific skills



<http://careers.physicstoday.org/post.cfm> **physicstoday** JOBS

## Ex situ variable angle spectroscopic ellipsometry studies on chemical vapor deposited boron-doped diamond films: Layered structure and modeling aspects

S. Gupta,<sup>1,a)</sup> A. Dudipala,<sup>1</sup> O. A. Williams,<sup>2</sup> K. Haenen,<sup>2</sup> and E. Bohannan<sup>3</sup>

<sup>1</sup>Department of Electrical and Computer Engineering, University of Missouri-Columbia, MO 65211, USA

<sup>2</sup>Institute for Materials Research (IMO), Hasselt University, BE-3590 Diepenbeek, Belgium and Division IMOMECA, IMEC vzw, BE-3590 Diepenbeek, Belgium

<sup>3</sup>Department of Chemistry and Materials Research Center, Missouri University of Science and Technology, Rolla, MO 65409, USA

(Received 6 May 2008; accepted 17 August 2008; published online 3 October 2008)

We report the optical property measurements on boron-doped diamond (BDD) films which were synthesized by microwave plasma-assisted chemical vapor deposition technique on Si (100) using methane in high hydrogen dilution and trimethylboron as precursors with varying boron concentration such that  $[B]/[C]_{\text{gas}} = 100, 500, 1000, 2000, 4000,$  and  $6467$  ppm. These BDD films were investigated using a rotating analyzer variable angle spectroscopic ellipsometry (SE) from the near IR to UV range (830–193 nm). By applying the conventional Bruggeman effective medium approximation and linear regression analyses to the raw SE data that is,  $[\psi(\lambda_i), \Delta(\lambda_i)]$  and pseudodielectric function  $(\langle \epsilon_r(\lambda_i) \rangle, \langle \epsilon_i(\lambda_i) \rangle)$ , we determined the most appropriate model fit. The SE modeling was performed through the normal and point-by-point fit methods combined with the coupled and uncoupled bulk and surface layer approaches providing the details about the thin films' microstructure in terms of the (a) multilayer (component and surface) structure and component layer thickness of the films, (b) volume fraction of constituents  $[f_{sp^3 C}, f_{sp^2 C}$  and void  $(f_v)$  in the component layer], (c) inhomogeneity of the structure along the growth axis and its variation with boron concentration, and (iv) surface roughness layer thickness  $(d_s)$  with dimensions less than the optical wavelength that is not otherwise available. A simplified three-layer structural model consisting of an interfacial layer, an intermediate (or bulk) layer, and a top surface roughness layer has been proposed, which simulates the ellipsometry data reasonably well with coupled point-by-point method. An estimator, i.e., mean squared error ( $\chi^2$ ), is used to assess the accuracy of the model fit. The results (surface roughness and constituents' fraction) obtained through SE modeling are also compared with those from atomic force microscopy (AFM) and Raman spectroscopy to validate the layered model employed. Typically, high surface roughness values around 6 nm were found for films grown under different boron concentrations which is almost five times smaller than determined from AFM. In this context, we determined an approximate linear relationship between these two variables. The relatively smaller surface roughness for BDD films indicates the combined role of boron-hydrogen (B, H) in diamond (C) while keeping the substrate temperature constant. We also discussed the variation of  $(f_v)$  and  $(f_{nd})$  for the bulk and surface layers with increasing boron concentration. © 2008 American Institute of Physics.

[DOI: 10.1063/1.2990058]

### I. INTRODUCTION

The word “diamond” inevitably brings to mind the coveted jewel. However, diamond is renowned amongst scientists and technologists for its impressive combination of exceptional physical (mechanical, thermal, electrical, electrochemical, and biological) properties offering multifunctionality that qualifies it to become the 21st century engineering material for multiple applications.<sup>1,2</sup> It is a wide bandgap semiconductor with  $E_g = 5.45$  eV, but when doped with boron the material becomes *p*-type semiconducting materials with very high room temperature electron and hole mobilities ( $\mu_h = 1800$  cm<sup>2</sup>/V s), thus enabling various elec-

tronic and electrochemical applications.<sup>3</sup> Besides being the hardest material known, optically diamond is transparent from the infrared (IR) to near ultraviolet (UV) region. The coexistence of these properties results in many potential technological applications including optical coatings, wide-band IR transmissive windows, devices with high-power optoelectronic switching devices,<sup>4</sup> high frequency field-effect transistors,<sup>4</sup> and high temperature and chemical corrosive operation.<sup>5</sup> In addition, the radiation hardness is another supreme advantage of diamond thus predestined its usage in the development of radiation hard electronics over the existing semiconductors (e.g., Si, GaAs, and AlGaIn) and outweighing SiC, widespread in (pulsed) power electronics.<sup>6</sup> The choice of diamond in “extreme/space environment” stems from the strongest C–C bonding strength, high thermal

<sup>a)</sup>Author to whom correspondence should be addressed. Electronic mail: guptas@missouri.edu.

conductivity to dissipate heat, low  $Z$  number and tissue equivalence, wide bandgap suppressing thermal carriers, and defect recombination/generation current, and these properties suggest that diamond is ideal for the fabrication of high performance UV light emitting diodes and deep UV ( $\leq 220$  nm) photodetectors while being visibly blind.<sup>7</sup> However, the development of diamond-based electronic devices is limited to single crystal.

The chemical vapor deposition (CVD) technology producing high-quality reproducible diamond thin films triggered enormous technological potential for multiple applications.<sup>8</sup> A variety of CVD techniques currently available use different activation sources to create plasma including thermal (hot-filament, flame), radiation (rf, microwave), electric fields (dc plasma), and others. Although these deposition techniques share some characteristics, each one of them has its own set of optimized processing conditions used to produce films with different sets of microscopic structure and physical properties. The various applications require that structural and physical properties be optimized (e.g., smoother surfaces, high-quality, mechanical hardness, optical transparency, and electrical conductivity) to fulfill a different function. Diamond thin films can possess electronic properties ranging from those of an insulator to semiconductor when doped from low to moderate levels and to those of a semimetal at higher doping levels.<sup>9</sup> The other technological challenge is the lack of suitable shallow donors and acceptors for efficient doping in diamond films resulting in traditional semiconducting diamond. When doped with boron (phosphorus), it yields an acceptor (donor) level at 0.37 eV ( $p$ -type) (Ref. 10) and 0.56 eV ( $n$ -type),<sup>10</sup> respectively. Though there are reports on shallow donor, but with little success, those claims are not substantiated.<sup>11</sup> For small atomic radius of boron compared to other potential dopants, it is readily incorporated into the dense ( $1.763 \times 10^{23}$  atoms  $\text{cm}^{-3}$ ) diamond lattice with high reproducibility and high enough concentration useful for electronic devices, while the Mott insulator-metal transition is predicted around  $2 \times 10^{20}$  B  $\text{cm}^{-3}$ .<sup>12,13</sup> Researchers continue its use as a  $p$ -type dopant, especially by its incorporation in CVD grown thin diamond films in the development of electrochemical microelectrodes<sup>14</sup> and diamond-based electronics.<sup>4</sup>

A great deal of attention has been given to the microscopic structural analyses of the surfaces and interfaces of thin films in order to establish *process-structure-property* relationships. In the realm of metrology, among several state-of-the-art techniques for optical characterization, spectroscopic ellipsometry (SE) proved to be quite influential for the past two decades in the semiconductor thin film process control and structural analysis<sup>15-17</sup> and for polycrystalline diamond thin films.<sup>18</sup> The importance of surfaces and interfaces has been known for many years in several areas of science and technology. In fact, the surfaces are important in everyday phenomena. Friction and surface tension leading and linking to other properties such as hydrophobicity and hydrophilicity are some good examples where fine control of surface microroughness becomes critical. Moreover, surface is becoming more important especially as miniaturization progresses where most of the material atoms are at the sur-

faces or interfaces instead of at the bulk. Though this is not the case in our present investigation, but for the applications we are seeking such as in electrochemical microelectrodes and radiation-hard electronic microdevices, the surface microroughness plays a vital role where detailed characterization becomes vital. Furthermore, microstructure is not only a classical theme in materials science but also a universal theme. What is usually done to add a new axis in controlling the microstructure is by adding dopants or varying process conditions to engineer and enable them for various applications. The ability to obtain optical data through SE is advantageous in scanning the parameter window for the desired properties, especially *in situ* mode.<sup>16</sup> The other advantages of SE are that it offers a nondestructive, noninvasive, fast, sensitive, and precise measurement technique. For instance, depending on the absorption coefficient of the material to be probed, the SE is equivalent to noninvasive depth profiling used for the microstructure analyses of hydrogenated amorphous silicon for solar cell application.<sup>17</sup>

Motivation to the present study has been derived from the optimization process of the chemical vapor deposited poly-/microcrystalline diamond films doped with boron facilitating diamond as  $p$ -type semiconducting in terms of microstructure and surface/interface. The SE has proven to be a useful tool in characterizing the surface quality of thin layers and is presently being widely used for the determination of surface microroughness of specularly smooth surfaces. CVD polycrystalline diamond, on the other hand, is usually rougher and may hamper its practicality toward several optical and electronic applications. In addition, CVD diamond growth invariably codeposits nondiamond or  $sp^2$ -bonded carbon. Doping diamond with either  $p$ -type (such as boron) or  $n$ -type (such as phosphorus and nitrogen) tends to smoothen the surfaces but at the cost of increasing nondiamond component. These process variations can be studied using vibrational spectroscopy techniques [IR and micro-Raman spectroscopy (RS)], but they are rather qualitative. The use of cross-sectional transmission electron microscopy (XTEM) in conjunction with electron energy loss spectroscopy (EELS) can be used to quantify the bonding configuration, but it is not a nondestructive technique. The SE on the other hand, that monitors the variation in polarization of the incident light interacting with the films' surface is informative, noninvasive, and provides detailed quantitative analyses of the constituents' fraction and optical constants.

It has been seen that microscopically rough surfaces, where the dimension of roughness is much less compared to the wavelength of the probing light, act as a single polarizable medium with refractive index less than the actual bulk material.<sup>19</sup> Thus, in SE the general approach in determining the microroughness is to assume that the surface layer is a homogeneous mixture of bulk material and void, and the effective dielectric constant of the surface layer is obtained from the dielectric constant of the bulk material and the volume fraction of void using an effective medium theory.

By fitting the experimental and theoretical ellipsometric spectra over a wide wavelength range, the volume fraction of void and the thickness of the surface layer can be determined. Though contradictions still exist regarding the choice

of a particular effective medium model over another and in actual interpretation of the thickness of the surface layer in the context of surface height irregularities, the above approach has been used quite successfully in many cases, particularly in characterization of surfaces of semiconductors (herein, *p*-type diamond).<sup>20,21</sup> The SE results are critically examined with other techniques measuring surface properties such as atomic force microscopy (AFM). Since SE measures the optical or dielectric constants, those results can also be corroborated with electrical *C-V* measurements and electrostatic force microscopy modeling. Another aspect of this work is that the surface microroughness variation with either growth parameters or monitoring its evolution *in situ* (kinetic or dynamic roughening) provides much needed information about their growth mechanism.

We employed *ex situ* SE for determining the layered structure of boron-doped diamond (BDD) thin films deposited by microwave plasma-assisted chemical vapor deposition (MWCVD). The complex refractive index of polycrystalline diamond,  $\tilde{N}=(\epsilon)^{1/2}=n-ik$ , where  $n$  is the refractive index and  $k$  is the extinction coefficient, generally differs from that of natural diamond. Since this is closely related to the microstructure of the film, it provides information about the distribution of bonding configurations and it is therefore an important parameter for practical applications. The early pioneering studies of diamond thin films demonstrated that the codeposition of  $sp^2$ -bonded C is a sensitive function of the process parameters.<sup>18</sup> Therefore, determination of the  $sp^2$  C phase and void network is of great interest because such bonding and structural defects lead to the degradation of the mechanical, optical, thermal, and electrical properties of diamond films. In addition, the diamond film surfaces are rough, typically consisting of well-defined crystalline facets and their sizes and shapes are related to the film deposition conditions. These surfaces determine to a large extent the diamond film properties. For applications such as UV sensors, electrochemical microelectrodes, and biosensing platforms, reduction of the surface roughness and the defect density (or nondiamond components) is crucial.<sup>17</sup> Other electronic applications that await a reliable *n*-type dopant for diamond will encounter similar issues.

A simplified three-layer structural model best described the diamond films is hereby studied. The ellipsometry data were simulated from the near IR (1.5 eV) to the near UV (5.0 eV) range for the determination of the surface roughness ( $d_s$ ), constituents' volume fraction ( $f_d, f_{nd}$ ), void fraction ( $f_v$ ), and overall thickness ( $d_{SE}$ ) of MWCVD grown BDD films. The underlying principle is that diamond thin films can be considered as heterogeneous materials consisting of primarily diamond and graphitic phases and the conventional Bruggeman effective medium approximation (EMA) can easily be employed.<sup>22</sup> Accordingly, we have the following theoretical framework:

$$\epsilon_j(\epsilon_j - \epsilon/\epsilon_j + 2\epsilon) = 0$$

$$\text{or } (\epsilon - \epsilon_h/\epsilon + K\epsilon_h) = \epsilon f_j(\epsilon_j - \epsilon_h/\epsilon_j + 2\epsilon_h),$$

where  $f_j$  are the relative volume fractions of the constituents  $j=A$  and  $B$ .  $K$  is a screening parameter and  $\epsilon_h$  is the host

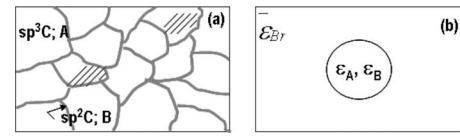


FIG. 1. (a) Microstructure of heterogeneous two-phase medium. (b) Corresponding random unit cell used to derive the effective dielectric permittivity within the Bruggeman theory.

dielectric function. For Bruggeman EMA,  $K=2$  and  $\epsilon=\epsilon_h$ , and a simple schematic is shown in Fig. 1.

## II. EXPERIMENTAL

Thin films of boron-doped poly-/microdiamond (BDD) used in the present study were synthesized in a commercial ASTeX 5 kW tubular microwave plasma-assisted CVD chamber on commercial Si(100) (0.05 cm thick, 1 cm<sup>2</sup> in area, 10<sup>-3</sup> Ω cm, Virginia Semiconductor Inc. Fredricksburg, VA) described in detail elsewhere.<sup>23,24</sup> Si wafers were ultrasonically rinsed in ethanol, and followed by seeding in solutions of ethanol and nanodiamond powder with a grain size of ~5 nm measured using AFM and dynamic light scattering.<sup>23</sup> However, it should be noted that these particles aggregate to sizes around 50–100 nm. Embedded diamond powder and the scratching residues introduced by ultrasonication serve nucleation sites. These films were deposited at 3500 W, using CH<sub>4</sub>/H<sub>2</sub>/trimethylboron [TMB; B(CH<sub>3</sub>)<sub>3</sub> for boron] source gas mixtures with [B]/[C]=100, 500, 1000, 2000, 4000, and 6467 ppm in gas phase, with total chamber pressure of ~40 Torr at the substrate temperature ~720 °C (estimated *via* an optical pyrometer), and the growth time of 35 min yielding approximate thickness of 0.2 μm. At the end of the deposition period, the CH<sub>4</sub> and TMB gas flows were stopped and the films were remained exposed to H<sub>2</sub> plasma at 2000 W and 40 Torr for additional 10 min. This postgrowth annealing in atomic hydrogen served to gasify any adventitious nondiamond  $sp^2$  carbon impurity, to minimize dangling bonds, and to fully hydrogenate the surface. The boron concentration for BDD films is estimated to range between 10<sup>19</sup>/cm<sup>3</sup> and 2 × 10<sup>21</sup>/cm<sup>3</sup> using Hall effect measurement technique for all of the samples.<sup>23</sup> Table I provides the detailed deposition parameters for all of the BDD samples along with sample IDs.

TABLE I. Deposition parameters for hydrogen terminated boron-doped poly-/microcrystalline diamond (BDD) thin films by MWCVD.

Substrate	Si (100)
Carbon precursor	1% CH <sub>4</sub> in high hydrogen
Microwave power (W)	2.45 GHz at 3 kW
Stage/substrate temperature ( $T_d$ )	750 °C
Deposition time	2 h
Total chamber pressure ( $P$ )	50 Torr
Boron precursor	100 ppm (2-61023B)
Trimethyl boron (TMB); [B]/[C] <sub>gas</sub>	500 ppm (2-61023)
concentration in gas phase (Sample ID)	1000 ppm (2-61026)
	2000 ppm (2-61020)
	4000 ppm (2-61019B)
	6467 ppm (2-61027)

The diamond films were analyzed in terms of morphology, structure, and physical (optical and electrical) properties using scanning electron microscopy; (SEM) (model Hitachi S4700), AFM (Veeco Model Multimode IV), micro-RS (model J-Y LabRAM ARAMIS), and *ex situ* variable angle SE (J. A. Woollam Inc. Model VASE). RS is used to analyze the structural phases and the bonding configurations in the films. The micro-Raman spectra were recorded in a backscattered configuration using a He–Ne laser radiation line  $\lambda_L = 633$  nm ( $E_L = 1.92$  eV) and the  $80\times$  objective of the Raman microprobe for all the measurements resulting in a probed area  $\sim 1\text{--}2\ \mu\text{m}^2$  with a minimum power  $\sim 10$  kW/cm<sup>2</sup> to avoid thermal degradation. All of the Raman spectra were fitted using Jandel Scientific PEAKFIT software (V. 4.0) based on Marquardt–Levenberg method.<sup>23</sup>

The *ex situ* ellipsometry measurements were carried out with a rotating analyzer ellipsometer (model VASE, J.A. Woollam Inc.) combined with autoretarder for higher accuracy in incident light polarization in the near IR to near UV range (830–193 nm) at an incident angle of  $65^\circ$  from the sample in the serially scanning mode with an energy interval of 0.05 eV. Linear regression analysis (LRA) methods employing the Marquardt–Levenberg<sup>25,26</sup> and conventional Bruggeman EMA have been used to simulate the *ex situ* SE data in different fitting procedures to determine the best fit using WVASE 32 software. In the analyses, the bulk optical function of the material components of the film microstructure, including *c*-Si, diamond component ( $sp^3$  C), and non-diamond component ( $sp^2$  C) as glassy carbon or graphite, was taken following Collins<sup>27</sup> and J. A. Woollams' materials database library. This ellipsometer is unable to distinguish the depolarization of the incident light beam upon reflection from an increase in the ellipticity.<sup>28,29</sup> However, this can be done by independently measuring the three ellipsometric parameters ( $N, S, C$ ) such that  $\beta = (N^2 + S^2 + C^2)^{1/2}$ , which can be properly calculated. This approach avoids the assumption that  $\beta$  remains equal to unity. Such a supposition implies a uniform film thickness over the probed area, which may not be the case sometimes. This in turn affects the calculated extinction coefficient (or imaginary part of refractive index,  $k$ ) more than the calculated thickness itself as it is the most sensitive parameter in the simulation. In an attempt to minimize errors due to light scattering, which increases with increasing photon energy, the analysis is restricted to the energy range from 1.5 to 5.0 eV despite the instrument can measure up to 6 eV.

### III. RESULTS AND DISCUSSION

#### A. Microscopy

Figure 2 shows the SEM and three-dimensional AFM images of the representative BDD samples grown with varying  $[B]/[C]$  concentration. A cross section of one of the diamond films grown with  $[B]/[C] = 1000$  ppm is also provided displaying a columnar structure of the diamond film. While SEM is qualitative providing the surface morphology characteristics of original films, the AFM provides a quantitative measure in terms of grain size ( $d$ ) and root mean square surface roughness ( $\sigma_{\text{rms}}$ ). The corresponding AFM analyses

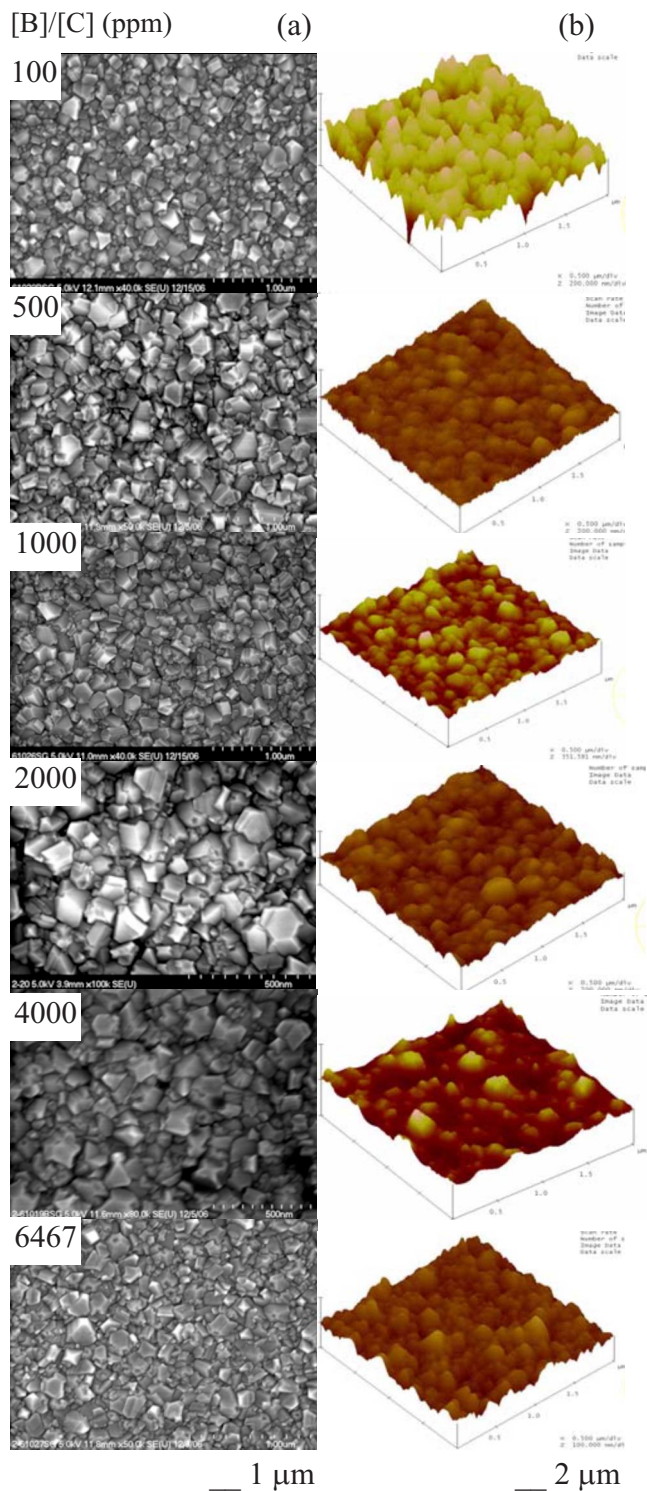


FIG. 2. (Color online) Shown are the (a) SEM and (b) three-dimensional AFM images of BDD films with varying  $[B]/[C]_{\text{gas}}$ .

are shown in Fig. 2 for all of the samples with varying boron concentration. For all of the samples, the SEM micrographs showed that the films are poly-/micromicrocrystalline with uniform surface coverage with no visible cracks, pinholes, or voids. The SEM micrographs also showed that the films are composed of well-faceted diamond crystallites with triangular growth habit or  $\langle 111 \rangle$  facets and grain size of  $>200$  nm for the least doped sample (100 ppm) that starts to turn relatively smaller grained with increasing boron doping concen-

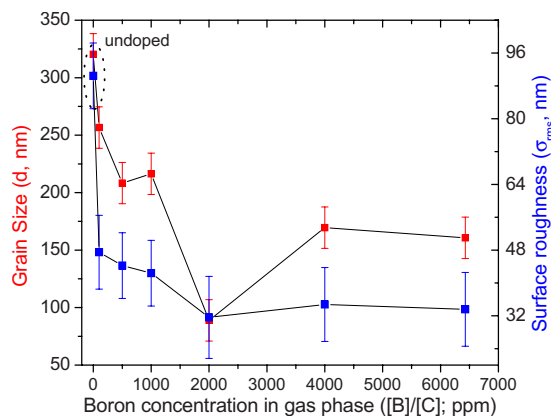


FIG. 3. (Color online) Plot of the variation of grain size ( $d$ ) and surface roughness ( $\sigma_{\text{rms}}$ ) estimated from AFM for the BDD films as a function of  $[B]/[C]_{\text{gas}}$ .

tration with feature sizes on the order of  $\leq 100$  nm. The AFM analyses (see Fig. 2) indicated that the average grain size ( $d$ ) varied from 250 nm  $\rightarrow$  100 nm for boron concentration from 100 to 2000 ppm and then increased to 160 nm with further increase in boron concentration to 6467 ppm with  $\pm 15$  nm (see Fig. 3). Likewise, the variation of the rms surface roughness ( $\sigma_{\text{rms}}$ ) values ranges 48 nm  $\rightarrow$  31 nm  $\rightarrow$  34 nm with increasing boron concentration with  $\pm 8$  nm (Fig. 3). These values are also compared with diamond films grown without boron and it is found that grain size is  $\sim 320$  nm and the surface roughness is  $\sim 90$  nm.<sup>23</sup> Note that the doping or impurity additions reduce the surface roughness in general. In comparison to N addition, the thermodynamic calculations suggested that they induce a transition from faceted to unfaceted morphology by activated species (possibly HCB and HCS analogous to HCN).<sup>11</sup> Despite these findings, the BDD films are much more stable and highly crystalline for relatively higher boron concentration as compared with those grown with  $n$ -type donor impurities.

## B. Raman spectroscopy

RS is widely used as a nondestructive analytical tool to characterize a variety of carbon-based materials.<sup>23</sup> Since RS can detect changes in behavior of C–C bonds, probing microstructural variation due to any treatment (plasma or chemical attack, doping impurity, and so forth) becomes much more informative. Visible RS ( $\lambda_L = 633$  nm or  $E_L = 1.92$  eV) is used to assess the lattice structure and to probe the changes in the structural bonding configurations for all of the BDD films with varying boron concentrations. Figure 4 displays the first-order micro-Raman spectra for all of BDD films with varying boron concentration. Given the importance of doping in diamond, it does not appear that there is any simple signature which can be used to assess the doping levels. Rather, the signatures which are subtle involve interactions between lattice vibrations and electronic continuum of states induced by the dopants. The Raman spectra in terms of peak position, peak widths, relative intensities, or integrated area of diamond films are quite sensitive to the bulk

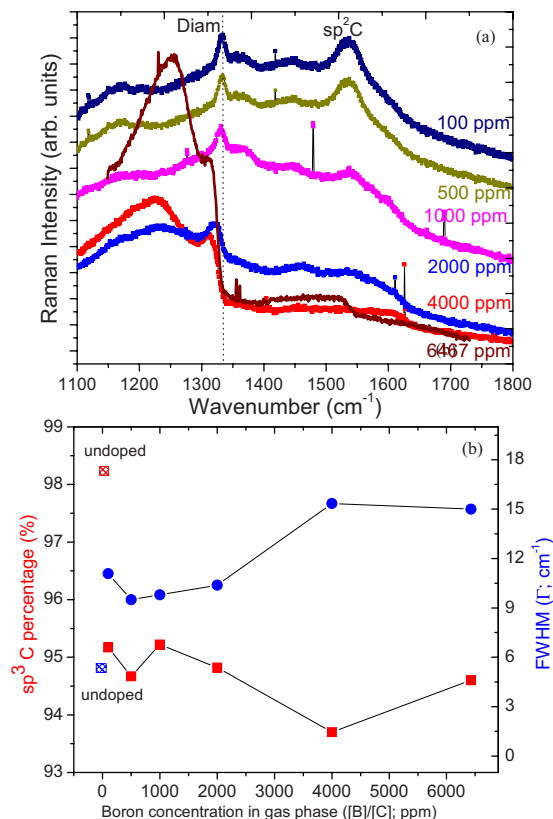


FIG. 4. (Color online) (a) Micro-Raman spectra of BDD films for varying  $[B]/[C]$  demonstrating the characteristic diamond (diam.) peak and nondiamond ( $sp^2$  C) band as well asymmetric Fano lineshape for the highest boron concentrations of 4000 and 6467 ppm. (b) Shown are the variation of  $sp^3$ -bonded carbon concentration ( $sp^3$  C%) and full-width at half maximum of characteristic diamond peak ( $\Gamma_{1332}$ ;  $\text{cm}^{-1}$ ) determined from micro-Raman spectra of BDD films for varying  $[B]/[C]_{\text{gas}}$ .

crystal structure, the boron-doping level, the internal stress (intrinsic and thermal), the defect density, and/or the presence of  $sp^2$ -bonded carbon impurity.<sup>30–32</sup>

Qualitatively, Raman spectral analyses revealed the zone center peak at  $1332$   $\text{cm}^{-1}$ , characteristic of diamond, which is the most intense and narrow for the lowest boron doping (i.e., 100 ppm). In addition to the relatively sharp Raman band at  $1332$   $\text{cm}^{-1}$ , the spectra have broad peaks at  $\sim 1200$  and  $1550$   $\text{cm}^{-1}$ . Minimal scattering intensity seen in the  $1500$ – $1600$   $\text{cm}^{-1}$  region is associated with the presence of nondiamond or  $sp^2$ -bonded carbon ( $sp^2$  C) phase. These spectral characteristics are consistent with heavily boron-doped films.<sup>33</sup> The band at  $\sim 1200$   $\text{cm}^{-1}$  peak appears to drastically increase in intensity for samples with higher boron concentrations (i.e., 4000 and 6467 ppm). Bernard *et al.*<sup>34</sup> proposed that these peaks have originated from the local vibrational modes of boron pairs reportedly formed in BDD films. These boron pairs increase in concentration as the total number of boron atoms in diamond increases which explains the enhanced intensity. Although the characteristic diamond peak position did not change significantly with boron doping, the lineshape becomes asymmetric for the highest B-doping levels of 4000 and 6467 ppm. This effect is due to Fano effect which is induced by quantum-mechanical interference between the discrete phonon states and electronic continuum.<sup>34</sup> The strongest effect appears to occur when the

doping level is  $\sim 2 \times 10^{20} \text{ cm}^{-3}$ , which corresponds to the onset of quasimetallic nature of the films, i.e., near zero activation energy and it is for samples higher than 1000 ppm of TMB in the present study.

The diamond peak observed at  $1332 \text{ cm}^{-1}$  is a symmetric Lorentzian at low boron concentration (i.e.,  $< 10^{20} / \text{cm}^3$ ) [Fig. 4(a)].<sup>23</sup> The relative height of the broad feature at  $1200 \text{ cm}^{-1}$  peak increases with increasing B concentration. This peak is related to the feature observed at  $1147 \text{ cm}^{-1}$  in intrinsic CVD diamond and attributed to disordered  $sp^3$ -bonded carbon ( $sp^3 \text{ C}$ ).<sup>8</sup> An approximate  $50 \text{ cm}^{-1}$  shift to higher frequency could be caused by the incorporation of the lighter boron into the disordered phase and for boron concentrations of  $\geq 10^{20} / \text{cm}^3$  the distinctive asymmetric Breit–Wigner–Fano or Fano lineshape is observed corresponding to  $[B] = 2 \times 10^{21} / \text{cm}^3$  and  $5 \times 10^{21} / \text{cm}^3$  for 4000 and 6467 ppm samples. Mathematically, the Fano lineshape is described by<sup>34,35</sup>  $I(\omega) = (q + \varepsilon)^2 / (1 + \varepsilon^2) + C$ , where  $\varepsilon = (\omega - \omega_0 - \Delta\omega_0) / \Gamma$  is a reduced frequency,  $q$  is the asymmetry parameter,  $\Gamma$  is a width,  $C$  is the background, and  $\Delta\omega_0$  is the shift of the diamond peak from its intrinsic value  $\omega_0 = 1332.5 \text{ cm}^{-1}$ . While small values of parameter  $q$  produces asymmetric lineshape, the Fano lineshape becomes Lorentzian as  $q \rightarrow \infty$ . Following the Fano lineshape analysis of the Raman spectra shown in Fig. 4(a), we obtained  $\Delta\omega_0 = -22.5$ ,  $q = 17.2$ , and  $\Gamma = 15.35$  and  $\Delta\omega_0 = -24.3$ ,  $q = 14.6$ , and  $\Gamma = 15.0$  for 4000 and 6467 ppm samples, respectively. The peak center shift to lower frequency is caused by a combination of the self-energy shift due to the Fano interaction and tensile stress in the lattice from the incorporation of substantial quantities of boron. The other important observation that can be derived from the Raman peaks is the decrease in the intensity of the peak around  $1200 \text{ cm}^{-1}$  irrespective of the boron concentration.

The change in lattice due to defects or impurity is also characterized by the phonon lifetimes ( $\tau$ ) reflected in the broadening ( $\Gamma$ ) of the characteristic peak at  $1332 \text{ cm}^{-1}$ . Alternatively, the linewidth results from the spread in phonon energy due to scattering caused by impurities and defects [i.e., grain boundaries (GBs)].<sup>31</sup> Therefore, the scattering event shortens the lifetime of the phonons, i.e.,  $\tau, \propto 1/\Gamma$  and thus broadens the characteristic diamond band in Raman spectra. On the basis of the experience with doped diamond films, we would expect a broadening of the diamond peak with increasing impurity concentration. The diamond peaks become broader ( $16 \text{ cm}^{-1} \rightarrow 32 \text{ cm}^{-1}$ ) with increasing boron concentration, as shown in Fig. 4(b). The characteristic diamond peak is close to intrinsic position  $\sim 1328.5 \text{ cm}^{-1}$  (for natural diamond,  $\omega_0 = 1332 \text{ cm}^{-1}$ ) pointing at a relatively small amount of tensile stress. The diamond content was evaluated from the ratio of the diamond peak area to that of the rest of the spectrum between  $1100$  and  $1800 \text{ cm}^{-1}$  while taking the Raman scattering cross section of non- $sp^3$  carbon to be 50 times that of diamond, as follows:  $f_{sp^3 \text{ C}}(\%) = [(50 \times I_d) / (50 \times I_d + I_{nd})] \times 100$ , where  $I_d$  is the area under the diamond peak and  $I_{nd}$  is the nondiamond ( $sp^2 \text{ C}$ ) curve. Figure 4(b) summarizes the variation of  $sp^3 \text{ C}$  concentration for all of the diamond samples as a function of boron concentration in addition to undoped diamond. In the

present investigations, we found that the percentage of  $sp^3 \text{ C}$  decreases slightly (96%–94%) with the increasing boron concentration. Interestingly enough, we did not observe dramatic change in their structural characteristics associated with the broad band at  $\sim 1550 \text{ cm}^{-1}$ . Further research is required to understand these findings and to gain insight into the observed behavior.

### C. Spectroscopic ellipsometry

To extend optical characterization, we employed *ex situ* SE and the variables psi and delta [ $\psi(\lambda_i), \Delta(\lambda_i)$ ] and pseudodielectric ( $\langle \varepsilon_r(\lambda_i) \rangle, \langle \varepsilon_i(\lambda_i) \rangle$ ) function from 1.5 to 5.0 eV were measured for BDD films. They all show the characteristic interference pattern depicted in Figs. 5–7 for a representative sample grown with  $[B]/[C]_{\text{gas}} = 4000$  ppm. These SE spectra were simulated under the presumption that the film composition is an aggregate mixture of  $sp^3$ - and  $sp^2$ -bonded carbon ( $sp^3 \text{ C}$ ,  $sp^2 \text{ C}$ ). For the  $sp^3 \text{ C}$  component, the optical constants of natural IIa type diamond were adopted, while for the  $sp^2$  component, the optical constants of glassy carbon or graphite were used. Models having a different number of layers and different compositions within these layers were applied to these ellipsometry data. Moreover, different approaches through the normal (Fig. 5) and point-by-point (Figs. 6 and 7) fit methods of coupled and uncoupled bulk and surface layers to find the most appropriate model were also used in an attempt to determine the details about the films' microstructure in terms of (a) multilayer (component and surface) layer thickness, (b) volume fraction of constituents [ $f_{sp^3 \text{ C}}$ ,  $f_{sp^2 \text{ C}}$ , and void ( $f_v$ ) in the component layer], (c) inhomogeneity along the growth axis and its variation with boron concentration, and (iv) surface roughness layer thickness ( $d_s$ ) with dimensions less than the optical wavelength that is not otherwise available.

A simplified three-layer structural model has been proposed that simulates the ellipsometry data reasonably well. The model also has an interfacial layer, which results from the silicon and diamond interface and is thus composed of silicon carbide (SiC). Last is the silicon substrate, assumed to be semi-infinite since the light does not bounce back after passing through it. Therefore, the total film thickness deduced from SE is defined as the summation of the three layers described for the model (see Figs. 5–7). The SE data are simulated by three different methods including normal (Fig. 5), uncoupled (Fig. 6), and coupled point-by-point (Fig. 7) fit methods for two different incident angles  $65^\circ$  and  $75^\circ$  (Fig. 7). In general, the degree of agreement between the model and the SE data can be evaluated from Figs. 5–7, where the continuous line corresponds to the simulation while the dotted lines correspond to the measured SE data. An unbiased estimator, i.e., mean squared error (MSE,  $\chi^2$ ), is used to assess the precision of the multilayered optical model following LRA.<sup>26</sup> In particular, it can be seen that the position and number of the extrema (maxima and minima) are well reproduced, which is an indication of accuracy of fit. The simulations were performed on a total of six samples grown with varying boron concentration and for all of the methods described above. In this study, we are particularly

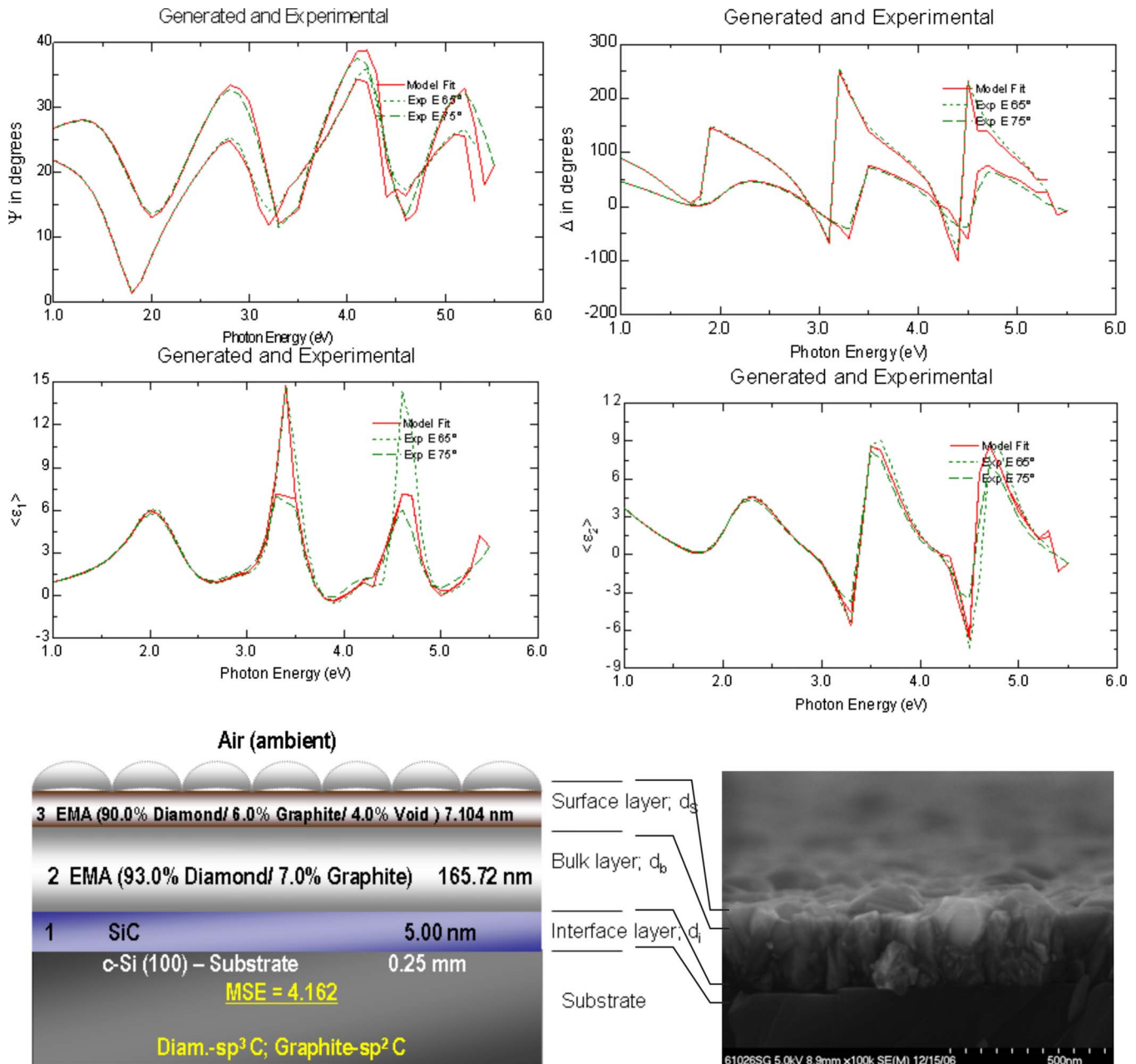


FIG. 5. (Color online) Representative *ex situ* SE data in terms of  $(\psi, \Delta)$  and pseudodielectric  $(\langle \epsilon_1 \rangle, \langle \epsilon_2 \rangle)$  function for one of the representative BDD thin films with  $[B]/[C]_{\text{gas}}=4000$  ppm. The dashes (---) are the raw data, while the solid line (—) is the best-fit simulation resulting from LRA of the experimental data using the Bruggeman EMA and a proposed three-layer structural model. The data indicate fit for the incident angles of  $65^\circ$  and  $75^\circ$ . The three-layer microstructure model and the optical model to describe the BDD film to simulate the *ex situ* SE spectra is also provided. The fitting is carried out in uncoupled normal fit mode. Notice that a cross-section SEM for a representative BDD film showing columnar morphology with surface corrugation is also shown for a better visualization relating the SE three-layered microstructure and optical model.

interested in the surface roughness ( $d_s$ ) and in the volume fraction of  $sp^3$ -bonded carbon ( $f_d$ ),  $sp^2$ -bonded carbon ( $f_{\text{nd}}$ ), and of voids ( $f_v$ ) in the bulk and surface layer of our films.

Tables IIa–IIc contain the simulation results for all six samples regarding the roughness ( $d_s$ ), bulk layer ( $d_b$ ) thickness, and corresponding MSE for all of the fitting methods and uncoupled and coupled approaches. These tables also provide the rms surface roughness ( $\sigma_{\text{rms}}$ ) determined from the AFM technique. On the other hand, Table III presents the volume fractions of the constituents and of voids in the bulk layer and dielectric function at a particular wavelength of 633 nm or photon energy  $E=1.92$  eV for two different inci-

dent angles  $65^\circ$  and  $75^\circ$ . We noted a variety of important observations as discussed in the following section.

The roughness values extracted from the SE measurements ( $d_s$ ) are compared with the AFM results (see Fig. 2). Similarly, the total film thickness measured through ellipsometry ( $d_{\text{SE}}=d_s+d_b+d_i \sim 195$  nm) is also tallied in Table II with those determined while growing the films ( $\sim 200$  nm). The overall film thicknesses measured by these two ways do agree reasonably well in coupled point-by-point fitting procedure with the least MSE thus giving another indication of the reliability of the three-layer optical model employed (Fig. 7). It is apparent that the surface roughness

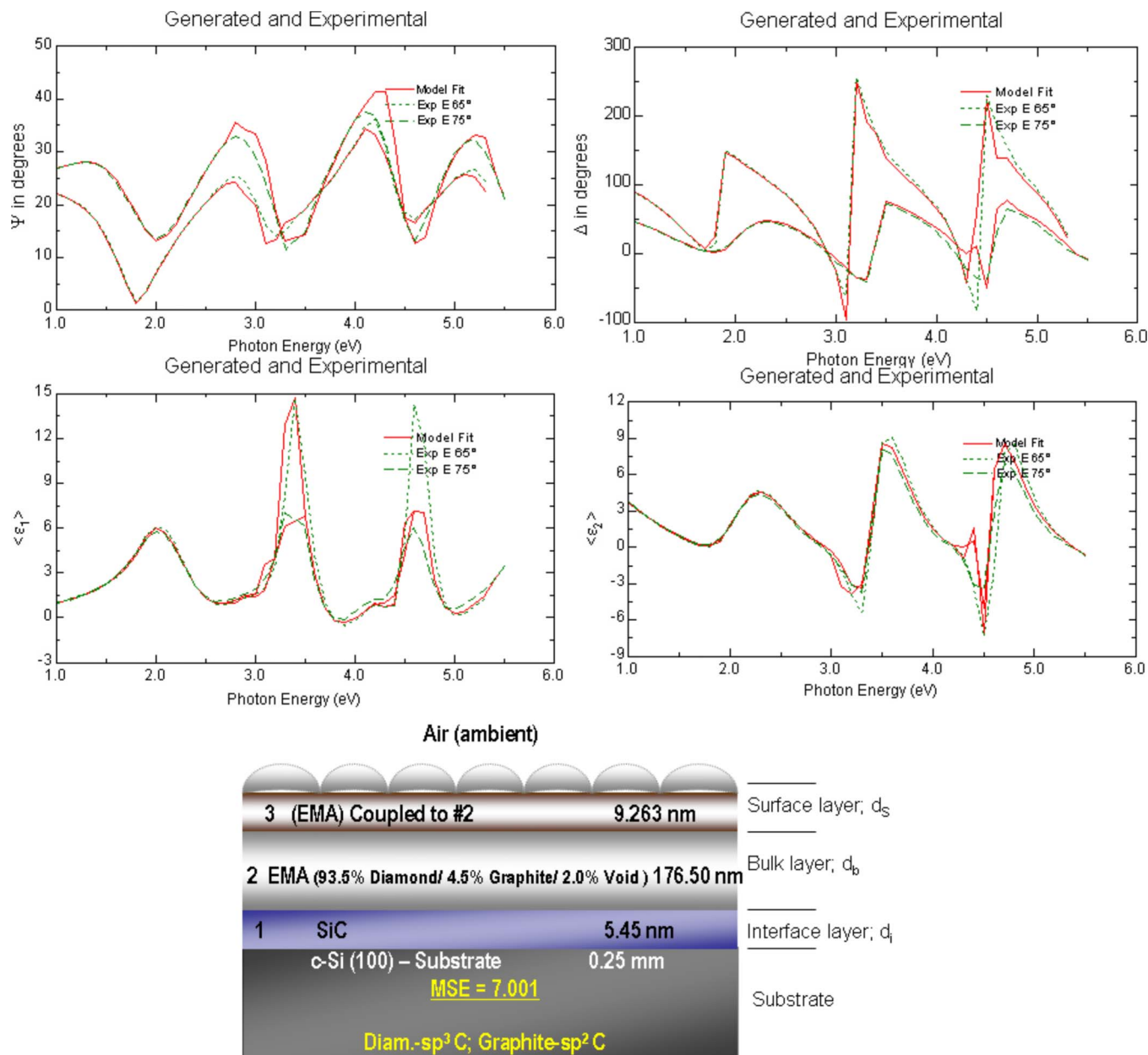


FIG. 6. (Color online) Representative *ex situ* SE data in terms of  $(\psi, \Delta)$  and pseudodielectric  $(\langle \epsilon_r \rangle, \langle \epsilon_i \rangle)$  function for one of the representative BDD thin films with  $[B]/[C]_{\text{gas}}=4000$  ppm. The dashes (---) are the raw data, while the solid line (—) is the best-fit simulation resulting from LRA of the experimental data using the Bruggeman EMA and a proposed three-layer structural model. The data indicate fit for the incident angles of  $65^\circ$  and  $75^\circ$ . The three-layer microstructure model and the optical model to describe the BDD film to simulate the *ex situ* SE spectra is also provided. The fitting is carried out in coupled normal fit mode.

measured by SE trend generally agrees with that estimated by AFM, but it is generally lower.<sup>36</sup> This may be due to the fact that SE is more sensitive to short surface-topography profile wavelengths (smaller than the photon wavelengths used and above which the effective medium theory breaks down), while AFM is sensitive to long surface profile wavelengths from  $0.1$  to  $1 \mu\text{m}$  within a scale of  $2 \times 2 \mu\text{m}^2$ . Thus AFM would be sensitive to those features seen in SEM (see Fig. 2) in the scale of  $1 \mu\text{m}$ , while SE will not. Since the AFM surface roughness values range between  $30$  and  $50$  nm, light scattering upon reflection may be causing depolarization effects during the ellipsometry measurements. This would result in the misinterpretation of the SE data leading to overestimated  $sp^2$  C volume fractions. In order to assess to

what extent this problem is affecting our results, we obtained the beta factor ( $\beta$ ), a measure of degree of depolarization<sup>37,38</sup> that is commonly assumed to be equal to unity when no significant depolarization effects are suspected. In our case, the  $\beta$  factor remained larger than  $0.98$  for the whole photon energy range of interest. This deviation from unity is so small that it should only have marginal effects on the estimated  $sp^2$  fractions ( $f_{\text{nd}}$ ). Quantitatively, we determined a general formula relating the average surface roughness layer values and those estimated from AFM for diamond films with varying boron concentration keeping other parameters the same, i.e.,  $\sigma_{\text{rms}}=39.15 \pm 1.17d_s$ . We also characterized low-frequency ( $400\text{--}800 \text{ cm}^{-1}$ ) Raman scattering and ob-

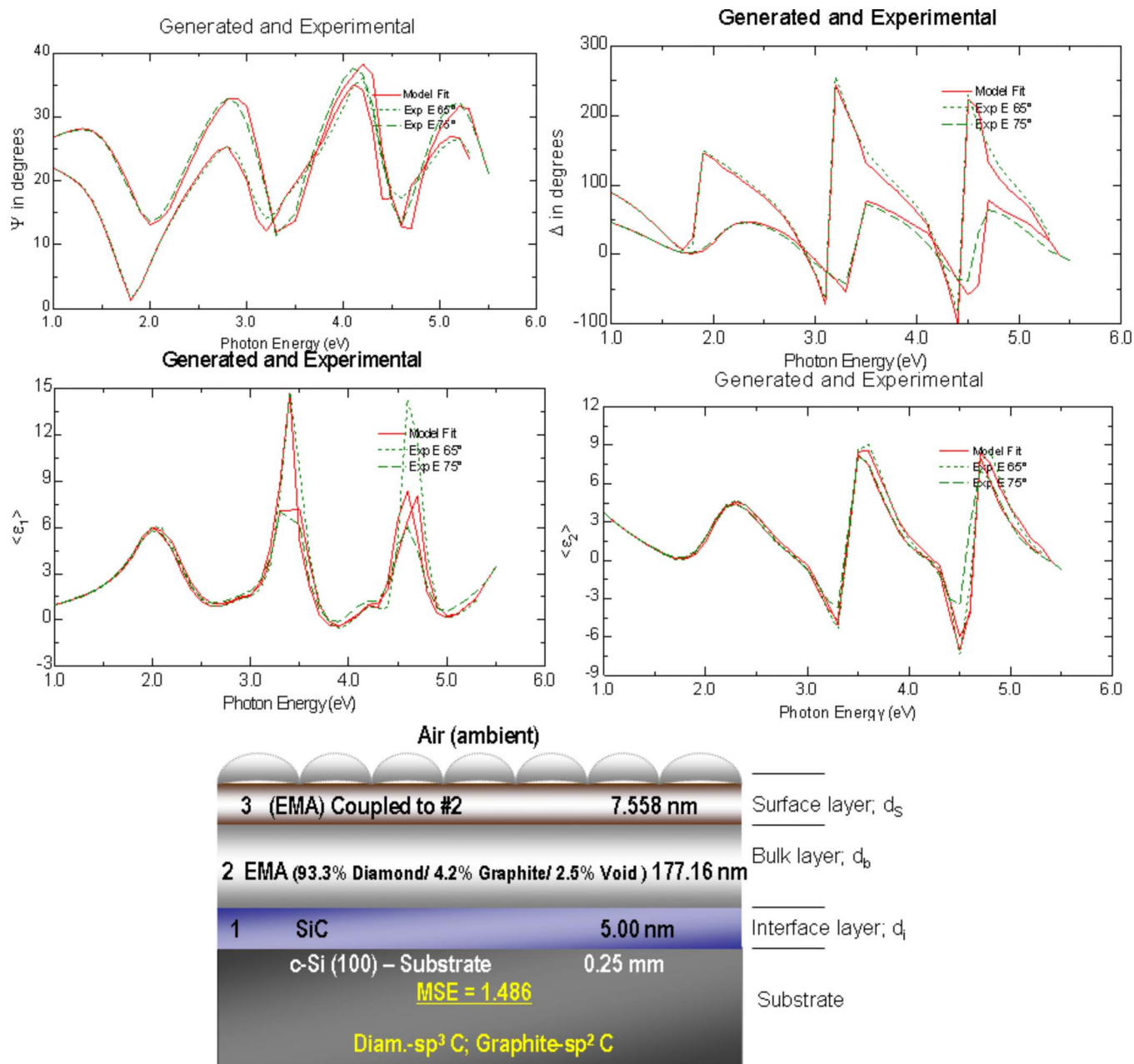


FIG. 7. (Color online) Representative *ex situ* SE data in terms of  $(\psi, \Delta)$  and pseudodielectric  $(\langle \epsilon_r \rangle, \langle \epsilon_i \rangle)$  function for one of the representative BDD thin films with  $[B]/[C]_{\text{gas}}=4000$  ppm. The dashes (---) are the raw data, while the solid line (—) is the best-fit simulation resulting from LRA of the experimental data using the Bruggeman EMA and a proposed three-layer structural model. The data indicate fit for the incident angles of  $65^\circ$  and  $75^\circ$ . The three-layer microstructure model and the optical model to describe the BDD film to simulate the *ex situ* SE spectra is also provided. The fitting is carried out in coupled point-by-point fit mode.

served a peak  $\sim 600$   $\text{cm}^{-1}$  (not shown), which may be likely due to the SiC phase. However, the thickness of this interface remains quite constant at 5 nm.

It is quite encouraging that the growth conditions employed yielded BDD films having  $sp^2$  C contents as low as those deposited at relatively higher temperatures of  $800\text{--}850$   $^\circ\text{C}$  and keeping the surface corrugations lower than 8 nm. Since at higher substrate temperatures surface mobilities increase, the atoms are more probable to find their most statistically equilibrated positions, and thus can form organized surfaces. However, neither the substrate temperature nor the boron and hydrogen alone were enough to reduce the overall surface roughness of these films. This result

suggests the combined role played by boron and hydrogen keeping the substrate temperature constant used to deposit diamond thin films. It was demonstrated that the boron doping increases  $sp^3$  C at the expense of the  $sp^2$  C component, increases the H capacity, weakens the C–H and C–CH<sub>3</sub> bond energy, and increases the energetic homogeneity of the film structure, which are interrelated with each other having a common origin. For instance, early work of Nashimura *et al.*<sup>39</sup> inferred that diamond crystal quality improved with increasing B concentration up to a gas-phase  $B/C$  ratio of  $\sim 400$  ppm. Likewise, Shinar *et al.*<sup>40</sup> found that the characteristic diamond Raman peak at  $1332$   $\text{cm}^{-1}$  was narrowed as a result of boron doping. Kaukonen *et al.*<sup>41</sup> reported im-

TABLE II. (a) EMA simulation results for a series of MWCVD deposited BDD thin films with varying boron concentration without coupled approach using normal fit method. The surface roughness from AFM is also presented. (b) EMA simulation results for a series of MWCVD deposited BDD thin films with varying boron concentration with coupled approach using normal fit method. (c) EMA simulation results for a series of MWCVD deposited BDD thin films with varying boron concentration with couple approach using point-by-point method.

		Bulk layer ( $d_b$ )				Surface layer ( $d_s$ )		
		[B]/[C] <sub>gas</sub> (ppm)	$f_d$ (%)	$f_{nd}$ (%)	$d_b$ (nm)	Surface roughness (nm)		Best fit ( $\chi^2$ )
(a)	Sample ID					From SE $d_s$ (nm)	From AFM ( $\sigma_{rms}$ )	
	2-61027	6467	93	7	165.718	7.10	31.23	4.162
	2-61019B	4000	94	6	172.014	6.49	33.61	8.079
	2-61020	2000	93	7	178.152	5.12	31.80	9.622
	2-61026	1000	93	7	170.429	4.65	42.40	10.590
	2-61023	500	94	6	175.119	7.84	43.57	9.594
	2-61023B	100	94	6	173.137	7.84	48.40	4.708

		Bulk layer				Coupled surface layer		Best fit ( $\chi^2$ )
		[B]/[C] <sub>gas</sub> (ppm)	$f_v$ (%)	$f_d$ (%)	$f_{nd}$ (%)	$d_b$ (nm)	$d_s$ (mm)	
(b)	Sample ID							
	2-61027	6467	2.0	92.50	4.50	176.50	9.263	7.001
	2-61019B	4000	2.0	94.00	4.00	171.05	8.283	9.597
	2-61020	2000	2.0	92.50	4.50	168.20	7.872	9.615
	2-61026	1000	2.5	92.84	4.66	193.46	9.060	11.420
	2-61023	500	2.5	92.79	4.66	180.46	9.399	8.885
	2-61023B	100	2.5	93.5	4.00	172.26	7.625	5.561

		Bulk layer				Coupled surface layer		Best fit ( $\chi^2$ )
		[B]/[C] <sub>gas</sub> (ppm)	$f_v$ (%)	$f_d$ (%)	$f_{nd}$ (%)	$d_b$ (nm)	$d_s$ (nm)	
(c)	Sample ID							
	2-61027	6467	2.50	92.3	4.20	177.156	7.558	1.486
	2-61019B	4000	2.00	94.0	4.00	175.000	7.789	1.015
	2-61020	2000	2.00	92.5	4.50	175.244	8.637	1.363
	2-61026	1000	2.25	92.1	4.65	206.223	8.985	1.062
	2-61023	500	2.55	92.8	4.65	180.465	9.399	1.054
	2-61023B	100	2.66	92.5	4.84	175.733	10.042	0.921

proved crystalline quality *via* B-doping monitored through (100) plane and enhanced electrical conductivity of the films. They also concluded that the model was inadequate for N-doping attributing this to the additional complexities arising due to solubility, surface diffusion, and lattice parameter mismatch, to name a few.<sup>41</sup> It is the inability of boron to participate in the growth of  $sp^2$  C or graphitic segments in the film and protuberations from the growing diamond surface thus assisting in producing a relatively even surface. Therefore, a boron atom in the C–B–H network presents a dead end to promote graphitic growth. As a consequence, the  $sp^2$  C contributions get bleached out with increasing boron doping level and the energetics in the film is changed accordingly. As a result, we also observed the improved quality on boron doping unlike N, P, and S impurity incorporations in diamond which increases the  $sp^2$  C content in the films.<sup>11</sup>

In general, from Table III, the  $f_{sp^2 C}$  values obtained from SE are usually smaller ( $\sim 93\%$ – $94\%$ ) than those obtained from RS ( $\sim 95\%$ – $98\%$ ), but the trends tally. They are

not expected to agree in absolute numbers since RS is insensitive to voids and inner surface  $sp^2$  C. It also follows from Table III that the lowest  $sp^2$  C contents are obtained for the films with the highest void densities, albeit smaller for BDD films than those of undoped diamond films.<sup>18</sup> Nevertheless, the high  $f_v$  for low  $sp^2$  C suggests that the nucleation occurring in the early stage of the growth has not completely coalesced. Thus the high  $sp^2$  C may be associated with the coalescence regions in the GBs suggested by Hong *et al.*<sup>42</sup> The  $f_v$  determined using SE decreases albeit small with increasing boron concentration (Table III). This implies that more surface coverages lead to denser films and it is in accord with the SEM measurements (see Fig. 2). In addition, the void fraction ( $f_v$ ) of the surface layer is relatively higher ( $\sim 4\%$ ), indicating denser bulk layer. With this three-layer structural model, the general features of the pseudo-optical spectra were also simulated and the results are presented in Table III at photon energy of 1.92 eV. The increase in  $\epsilon_i$  with photon energy and with decreasing boron concentration indicates

TABLE III. (a) EMA simulation results for a series of MWCVD deposited BDD thin films with varying boron concentration with coupled approach using normal fit method. (b) EMA simulation results for a series of MWCVD deposited BDD thin films with varying boron concentration with coupled approach using point-by-point method.

		Bulk layer ( $d_b$ )			$\epsilon = \epsilon_r - i\epsilon_i$ ( $E=1.92$ eV)				
		[B]/[C] <sub>gas</sub> (ppm)	$f_v$ (%) (void)	$f_d$ (%) (diamond)	$f_{nd}$ (%) (nondiamond)	Fitting		Expt.	
(a)	Sample ID					65°	75°	65°	75°
	2-61027	6467	2.0	93.50	4.50	5.426– $i0.631$	6.012– $i1.884$	5.464– $i0.580$	5.784– $i1.817$
	2-61019B	4000	2.0	94.00	4.00	4.753– $i1.430$	3.983– $i3.588$	4.563– $i1.632$	4.446– $i3.786$
	2-61020	2000	2.0	93.50	4.50	6.645– $i5.391$	6.687– $i1.483$	7.723– $i5.261$	6.940– $i1.085$
	b2-61026	1000	2.5	92.84	4.66	1.708– $i3.676$	1.352– $i0.700$	1.310– $i4.070$	1.535– $i0.380$
	2-61023	500	2.5	92.79	4.66	8.435– $i3.933$	8.378– $i2.987$	9.934– $i2.753$	7.766– $i3.644$
	2-61023B	100	2.5	92.5	4.00	5.477– $i6.232$	6.107– $i6.353$	6.002– $i6.384$	5.898– $i6.259$

		Bulk layer ( $d_b$ )			$\epsilon = \epsilon_r - i\epsilon_i$ ( $E=1.92$ eV)				
		[B]/[C] <sub>gas</sub> (ppm)	$f_v$ (%) (void)	$f_d$ (%) (diamond)	$f_{nd}$ (%) (nondiamond)	Fitting		Expt.	
(b)	Sample ID					65°	75°	65°	75°
	2-61027	6467	2.50	92.3	4.20	5.421– $i0.640$	5.988– $i1.444$	5.464– $i0.580$	5.784– $i1.817$
	2-61019B	4000	2.00	94.0	4.00	4.427– $i1.502$	4.869– $i4.212$	4.563– $i1.632$	4.446– $i3.786$
	2-61020	2000	2.00	93.5	4.50	6.583– $i5.406$	6.695– $i1.490$	7.723– $i5.261$	6.940– $i1.085$
	2-61026	1000	2.25	93.1	4.65	1.177– $i3.733$	1.353– $i0.707$	1.310– $i4.070$	1.535– $i0.380$
	2-61023	500	2.55	92.8	4.65	8.435– $i3.910$	8.377– $i3.056$	9.934– $i2.753$	7.766– $i3.644$
	2-61023B	100	2.66	92.5	4.84	5.428– $i6.239$	6.128– $i6.333$	6.002– $i6.384$	5.898– $i6.259$

that the material exhibits a bandgap, partially due to the increase in  $sp^2$  C fraction as mentioned above. Moreover, due to the high density,  $3.51 \text{ g/cm}^3$ , the relative dielectric constant ( $\epsilon_r$ ) of diamond is 5.68.<sup>43</sup> For a particular set (100 and 6467 ppm), both the  $\epsilon_r$  and  $\epsilon_i$  shifts downward at both the incident angles. The relatively small discrepancy is due to the fact that the films consist of mixed  $sp^3$ - and  $sp^2$ -bonded carbon phases and therefore the resulting value and its variation with boron concentration are effective dielectric constants. Both the crystallite size and the extent of microstructural order also have important implications on these findings, as reported earlier for similar nature of BDD films using electrostatic force microscopy technique.<sup>24</sup> Accordingly, BDD films' surfaces have contrast of conductive regions (areas much less than  $1 \mu\text{m}^2$  in diameter), which were uniformly distributed. Alternatively, there is a presence of “positive-negative-positive” phase shift along the line section that indicates the presence of “insulating-conducting-insulating” phases, although qualitative. Furthermore, the increase in relative dielectric constant is attributed to the change in the crystal field caused by surface bond contraction of the poly-/microcrystallites and to the conjugated double bonds or graphitic phase with varying boron concentration.<sup>24</sup>

#### IV. CONCLUSION

In summary, *ex situ* SE from the near IR to near UV range (1.5–5.0 eV) was employed to investigate the layered structure of boron-doped polycrystalline diamond thin films grown by MWCVD with varying boron to carbon concentration in gas phase. A simplified three-layer structural model

was found to be reasonably well for simulating the ellipsometry spectra satisfactorily. The model consists of an interfacial layer, a bulk layer, and the top surface roughness layer. The raw SE data were fitted with various approaches including normal fit and point-by-point fit in coupled and uncoupled bulk and surface layer methods. We found that coupled point-by-point method was one of the most appropriate fit as evaluated using accuracy of fit estimator. The results obtained through SE modeling in terms of surface roughness and constituents' fraction are also compared with those from AFM and RS to validate the model employed and the overall thicknesses tallied reasonably well. The bulk void fractions decrease albeit small with increasing boron concentration function. This indicates the growth of denser films with higher boron concentration and is in accord with SEM measurements. We also discussed these findings with varying process condition including boron concentration in terms of interplay of boron-hydrogen in diamond in estimating the various parameters ( $f_{sp^3 \text{ C}}$ ,  $f_{sp^2 \text{ C}}$ , and  $f_v$  dielectric constants). Some of these results tallied with our previous reports on similar BDD films that were characterized using electrostatic force microscopy which suggests that the area of high conductivity density correlates with a high boron doping level along with electrical conductivity heterogeneity of boron-doped poly-/microcrystalline diamond surfaces. The presence of a “positive-negative-positive-negative” phase shift along the line section indicates the presence of “insulating-conducting-insulating-conductive” phases, respectively, though qualitative. This pioneering study served to illustrate the layered structural properties of BDD films and these findings may highlight some of the important factors influencing

physical (electrical, field emission, and electrochemical) properties for various applications, such as metal recovery and oxidation of organic residues contained in industrial wastewaters.

## ACKNOWLEDGMENTS

S.G. and A.D. are thankful to Dr. S. Gangopadhyay (ECE Department, University of Missouri-Columbia) for using VASE system and Dr. X. Han (Brewer Science, Rolla) for using Raman spectrometer. S.G. and A.D. acknowledge financial support in part by startup funds, Research Council awards, and MU Curators' Grant-in-Aid. O.A.W. and K.H. provided the BDD films and thank the financial support from the EU FP6 Marie Curie RTN "DRIVE" (MRTN-CT-2004-512224), by the Research Programs G.0068.07 and G.0430.07 of the Research Foundation-Flanders (FWO), and the IAP-P6/42. K.H. is a postdoctoral researcher under the FWO Award.

- <sup>1</sup>A. T. Collins, in *The Properties and Growth of Diamond*, edited by G. Davies (Inspec, London, 1994).
- <sup>2</sup>R. Kalish, in *Properties of Diamond*, edited by G. Davies (Inspec, London, 1994).
- <sup>3</sup>J. Isberg, J. Hammersberg, E. Johansson, T. Wikström, D. J. Twitchen, A. J. Whitehead, S. E. Coe, and G. A. Scarsbrook, *Science* **297**, 1670 (2003).
- <sup>4</sup>A. Aleksov, E. Kohn, J. Kusterer, and A. Denisenko, *Diamond Relat. Mater.* **12**, 391 (2003).
- <sup>5</sup>A. E. Fischer, Y. Show, and G. M. Swain, *Anal. Chem.* **76**, 2553 (2004).
- <sup>6</sup>I. V. Grekhov and G. A. Mesyats, *Phys. Usp.* **48**, 703 (2005).
- <sup>7</sup>M. Y. Liao, Y. Koide, and J. Alvarez, *Appl. Phys. Lett.* **88**, 033504 (2006).
- <sup>8</sup>S. Gupta, R. S. Katiyar, D. R. Gilbert, R. K. Singh, and G. Morell, *J. Appl. Phys.* **88**, 5695 (2000).
- <sup>9</sup>J. A. Garrido, C. E. Nebel, M. Stutzmann, E. Gheeraert, N. Casanova, E. Bustarret, and A. Deneuve, *Diamond Relat. Mater.* **11**, 347 (2002).
- <sup>10</sup>R. Kalish, *Diamond Relat. Mater.* **10**, 1749 (2001).
- <sup>11</sup>S. Gupta, B. R. Weiner, and G. Morell, *J. Mater. Res.* **18**, 363 (2002).
- <sup>12</sup>A. W. S. Williams, E. C. Lightowers, and A. T. Collins, *J. Phys. C* **3**, 1727 (1970).
- <sup>13</sup>E. Bustarret, E. Gheeraert, and K. Watanabe, *Phys. Status Solidi A* **199**, 9 (2004) and references therein.
- <sup>14</sup>A. E. Fischer, Y. Show, and G. M. Swain, *Anal. Chem.* **76**, 2553 (2004).
- <sup>15</sup>P. Chindaudom and K. Vedam, in *Optical Characterization of Real Films and Surface*, edited by K. Vedam (Academic, New York, 1994), pp. 191–247.

- <sup>16</sup>D. E. Aspnes, in *Handbook of Optical Constants of Solids*, edited by E. D. Palik (Academic, New York, 1985), pp. 89–112.
- <sup>17</sup>S. Gupta, B. R. Weiner, and G. Morell, *J. Vac. Sci. Technol. A* **23**, 1668 (2005).
- <sup>18</sup>S. Gupta, B. R. Weiner, and G. Morell, *J. Appl. Phys.* **90**, 1280 (2001).
- <sup>19</sup>E. Aspnes, J. B. Theeten, and F. Hottier, *Phys. Rev.* **B20**, 3292 (1974).
- <sup>20</sup>P. Petrik, T. Lohner, M. Fried, L. P. Biro, N. Q. Khanh, J. Gyulai, W. Lwhnetry, C. Schneider, and H. Ryssel, *J. Appl. Phys.* **87**, 1734 (2000).
- <sup>21</sup>L. Lai and E. A. Irene, *J. Appl. Phys.* **86**, 1729 (1999).
- <sup>22</sup>D. A. G. Bruggeman, *Ann. Phys.* **24**, 636 (1935).
- <sup>23</sup>S. Gupta, O. A. Williams, R. J. Patel, and K. Haenen, *J. Mater. Res.* **21**, 3037 (2007).
- <sup>24</sup>S. Gupta, O. A. Williams, and E. Bohannon, *J. Mater. Res.* **22**, 3014 (2007).
- <sup>25</sup>D. W. Marquardt, *J. Soc. Ind. Appl. Math.* **11**, 431 (1963); K. Levenberg, *Appl. Phys. Lett.* **65**, 1641 (1994).
- <sup>26</sup>W. H. Press, S. A. Teukolosky, W. T. Vetterling, and B. P. Flannery, in *Numerical Recipes in Fortran 77* (Cambridge University, Cambridge, England, 1992), Vol. 1, Chap. 15, p. 650.
- <sup>27</sup>B. Hong, J. Lee, R. W. Collins, Y. Kuang, W. Drawl, R. Messier, T. T. Tsong, and Y. F. Strausser, *Diamond Relat. Mater.* **6**, 55 (1997).
- <sup>28</sup>G. E. Jellison, Jr. and J. W. McCamy, *Appl. Phys. Lett.* **61**, 512 (1992).
- <sup>29</sup>J. Lee, P. I. Rovira, I. An, and R. W. Collins, *Appl. Phys. Lett.* **72**, 900 (1998); *Rev. Sci. Instrum.* **69**, 1800 (1998).
- <sup>30</sup>J. A. Bennett, J. Wang, Y. Show, and G. M. Swain, *J. Electrochem. Soc.* **151**, E306 (2004).
- <sup>31</sup>S. Praver and R. J. Nemanich, *Proc. R. Soc. London, Ser. A* **362**, 2537 (2004).
- <sup>32</sup>J. W. AgerIII, W. Walukiewicz, M. McMilluskey, M. A. Plano, and M. I. Landstrass, *Appl. Phys. Lett.* **66**, 616 (1995).
- <sup>33</sup>P. Pruvost and A. Deneuve, *Diamond Relat. Mater.* **10**, 531 (2001).
- <sup>34</sup>M. Bernard, C. Baron, and A. Deneuve, *Diamond Relat. Mater.* **13**, 896 (2004).
- <sup>35</sup>U. Fano, *Phys. Rev.* **124**, 1886 (1961).
- <sup>36</sup>J. Koh, Y. Lu, C. R. Wronski, Y. Kuang, R. W. Collins, T. T. Song, and Y. E. Strausser, *Appl. Phys. Lett.* **69**, 1297 (1998).
- <sup>37</sup>G. E. Jellison, Jr. and J. W. McCamy, *Appl. Phys. Lett.* **61**, 512 (1992).
- <sup>38</sup>J. Lee, P. I. Rovira, I. An, and R. W. Collins, *Appl. Phys. Lett.* **72**, 900 (1998).
- <sup>39</sup>K. Nashimura, K. Das, and J. T. Glass, *J. Appl. Phys.* **69**, 5 (1991).
- <sup>40</sup>R. Shinar, M. Leksono, and H. R. Shanks, *J. Vac. Sci. Technol. A* **11**, 569 (1993).
- <sup>41</sup>M. Kaukonen, P. K. Sitch, G. Jungnickel, R. M. Nieminen, S. Pöykkö, D. Porezag, and Th. Frauenheim, *Phys. Rev. B* **57**, 9965 (1998).
- <sup>42</sup>J. Lee, R. W. Collins, B. Hong, R. Messier, and Y. E. Strausser, *J. Vac. Sci. Technol. A* **15**, 1929 (1997).
- <sup>43</sup>H. Sakaue, N. Yoshimura, S. Shingubara, and T. Takahagi, *Appl. Phys. Lett.* **83**, 2226 (2003).